Electrochemical Impedance Spectroscopy of All-Perovskite Tandem Solar Cells

Bart Roose[1*], Krishanu Dey[2], Melissa R Fitzsimmons,[1] Yu-Hsien Chiang[2], Petra J Cameron[3], Samuel D Stranks[1,2*]

[1] Department of Chemical Engineering and Biotechnology, University of Cambridge, Philippa Fawcett Drive, Cambridge, CB3 0AS, UK

[2] Department of Physics, Cavendish Laboratory, University of Cambridge, 19 JJ Thomson Avenue, Cambridge, CB3 0HE, UK

[3] Department of Chemistry, University of Bath, Claverton Down, Bath, BA2 7AY, UK

E-mail: br340@cam.ac.uk; sds65@cam.ac.uk

Abstract

This work explores electrochemical impedance spectroscopy to study recombination and ionic processes in all-perovskite tandem solar cells. We exploit selective excitation of each sub-cell to enhance or suppress the impedance signal from each sub-cell, allowing study of individual tandem sub-cells. We use this selective excitation methodology to show that the recombination resistance and ionic time constants of the wide gap sub-cell are increased with passivation. Furthermore, we investigate sub-cell-dependent degradation during maximum power point tracking and find an increase in recombination resistance and a decrease in capacitance for both sub-cells. Complementary optical and external quantum efficiency measurements indicate that the main driver for performance loss is the reduced capacity of the recombination layer to facilitate recombination due to the formation of a charge extraction barrier. This methodology highlights electrochemical impedance spectroscopy as a powerful tool to provide critical feedback to unlock the full potential of perovskite tandem solar cells.

Table of contents graphic

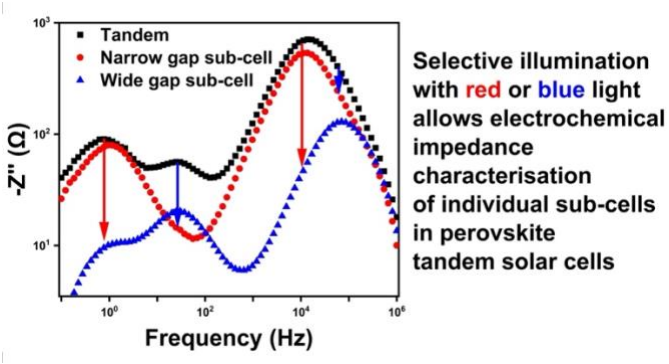

Perovskite solar cells (PSCs) have made great progress since the first report in 2009.[1] Record lab-scale power conversion efficiency (PCE) is practically on-par with established silicon technology,[2] and further improvements are still expected.[3] This rapid development can be attributed to the excellent optoelectronic properties of halide perovskites and their compatibility with inexpensive processing methods.[4,5] PSCs show potential to be fabricated cost-effectively using high-throughput methods[6] in geographically distributed facilities.[7]

The bandgap of metal halide perovskites can be tuned by altering the chemical composition, making these materials strong candidates for tandem solar cells.[8–13] A tandem solar cell consists of two sub-cells stacked on top of each other. Each sub-cell absorbs a different region of the solar spectrum,

which allows tandem solar cells to harvest a broader range of wavelengths more efficiently than a single absorber alone. In all-perovskite tandem solar cells, the narrow bandgap sub-cell typically uses an alloyed lead/tin pure iodide perovskite ($APb_xSn_{1-x}I_3$), with a bandgap of ~1.2-1.25 eV. The wide bandgap sub-cell uses an $APb(I_xBr_{1-x})$ perovskite with bromide fractions up to 40% and a bandgap of ~1.7-1.8 eV.[14] The radiative efficiency limit of a tandem solar cell is ~45%, compared to ~33% for a single junction (SJ) solar cell.[15] Tandem solar cells can thus significantly reduce the $/W cost of photovoltaics and further speed up the renewable energy transition.[16] Remarkable progress in all-perovskite tandem efficiency has been achieved by improving the wide bandgap sub-cell,[17,18] the narrow bandgap sub-cell,[14,19,20] and the recombination junction.[21] However, all-perovskite tandems have only recently surpassed SJ PSCs in PCE (26.0% for SJ versus 29.1% for all-perovskite tandem solar cells),[22] and are still far from practical efficiency limits.[15] A better understanding of the device properties is essential to further increase performance in a systematic, consistent and rational fashion. However, tandem solar cells bring new challenges through the increased complexity of these devices compared to SJ cells,[23] and new approaches need to be developed to study individual sub-cells or interfaces within the tandem stack.[18]

Electrochemical Impedance Spectroscopy (EIS) is a powerful characterisation technique that can provide insights into electrical and electrochemical processes that occur during device operation. Typically, a 5-10 mV sinusoidally oscillating voltage is applied in addition to a DC voltage bias. The resulting sinusoidally varying current output is measured as a function of the frequency of the sinusoidally oscillating voltage. By measuring the amplitude and phase shift of the current with respect to the applied voltage the impedance can be calculated. The excitation signal perturbs the device, and as the time it takes the system to respond (relaxation time) is process-specific, allowing the distinction of processes occurring at different timescales. More information can be extracted from the spectrum by modelling with an equivalent circuit (EC), and the values of the resulting parameters can provide information on the underlying physical nature of these different processes.[24–28] EIS has been used extensively in SJ perovskite solar cells to study processes such as surface recombination and charge collection efficiency,[27] interfacial and ionic reactions,[29] and activation energies for ionic motion.[30,31] However, EIS has not yet been applied to perovskite tandem solar cells.

Here, electrochemical impedance spectroscopy (EIS) is explored to characterise all-perovskite tandem solar cells. We show that tandem EIS spectra acquired under standard measuring conditions (i.e. full spectrum illumination) are complex and hard to resolve for individual sub-cells. In order to better understand the EIS of the tandem cell, we have measured EIS for wide gap and narrow gap SJ cells. We see the expected dependence of the spectra on light intensity, where the magnitude of the impedance signal increases with decreasing intensity at all frequencies, while simultaneously there is a shift in the frequency at which the impedance reaches a maximum.[30,32] Making use of the different bandgaps of the narrow and wide bandgap sub-cells, we use modified illumination spectra to selectively excite individual sub-cells in the tandems. This allows us to extract sub-cell-selective information, as we show that the impedance response is dominated by the current-limiting sub-cell. Increasing the intensity of the wavelengths that are only absorbed by one sub-cell ensures that the current is limited by the second sub-cell, allowing accurate time constants to be extracted for the second sub-cell. We use this selective illumination approach to study the effects of passivation of the wide gap sub-cell on the electronic recombination and ionic time constants of an all-perovskite tandem. We find that the high frequency recombination resistance and low frequency ionic time

constants of the wide gap sub-cell are increased with passivation, while those of the narrow gap remain largely unchanged. In addition, we studied the effects of operating an all-perovskite tandem at the maximum power point for 24 hours, during which the tandem efficiency decreases to ~75% of the starting efficiency. At the same time, an increase in electronic recombination time constant is found for both sub-cells. Complementary photoluminescence (PL), UV/Vis absorption and external quantum efficiency (EQE) measurements indicate that the recombination junction becomes less efficient under operation. We demonstrate the versatility of the selective illumination EIS method to better understand all-perovskite tandems, allowing targeted approaches to further improve efficiency and stability.

All-perovskite tandem solar cells were fabricated building on previous work,[14,33] with perovskite absorber layers solution-processed in device stacks consisting of ITO / [2-(9*H*-Carbazol-9-yl)ethyl]phosphonic acid (2PACz) / $Cs_{0.25}FA_{0.75}Pb(I_{0.767}Br_{0.233})$ wide gap perovskite / Propane-1,3-diammonium iodide ($PDAI_2$) / C60 / SnO_x / Au / PEDOT:PSS / $Cs_{0.15}FA_{0.85}Pb_{0.5}Sn_{0.5}I_3$ narrow gap perovskite / Ethane-1,2-diammonium iodide ($EDAI_2$) / C60 / BCP / Cu (see inset Figure 1a). An average power conversion efficiency (PCE) of ~22% and a champion PCE of 23.8% (Figure 1a, Table 1) was achieved. Short circuit currents (J_{SC}) match well between *J-V* and EQE measurements (Figure S1). Performance loss of the devices is negligible on timescales (~10 minutes) that are required to record an electrochemical impedance spectrum (Figure 1b).[25] Wide gap (ITO / 2PACz / wide gap perovskite / $PDAI_2$ / C60 / BCP / Cu) and narrow gap (ITO / PEDOT:PSS / narrow gap perovskite / $EDAI_2$ / C60 / BCP / Cu) SJ devices, analogous to the tandem sub-cells, were fabricated (performance statistics in Table S1) to compare EIS signals between tandems and SJs. Note that these SJ devices use identical absorber and charge transport layers as the corresponding tandem sub-cells.

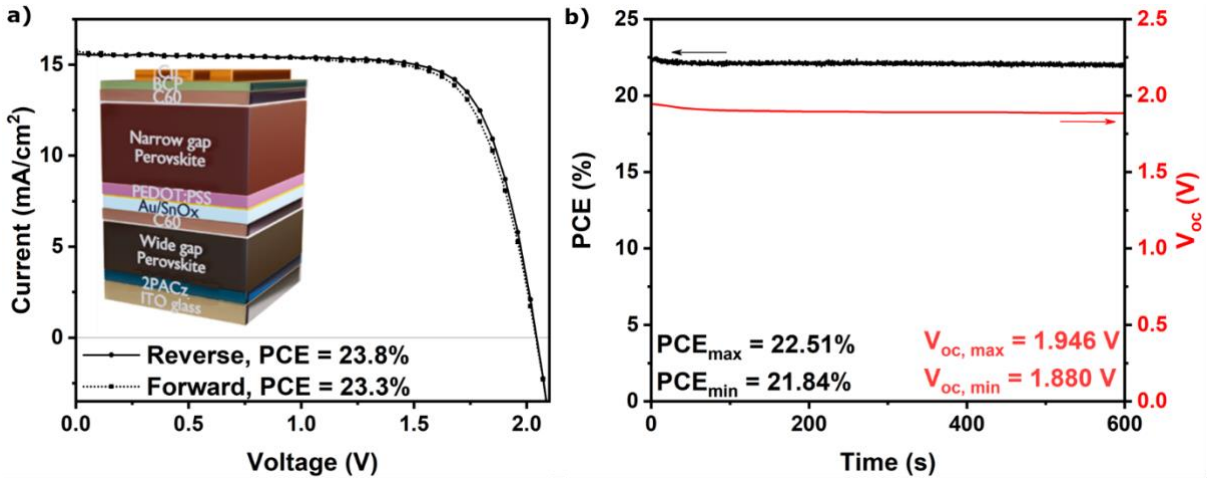

Figure 1: *a)* J-V *curve of champion efficiency all-perovskite tandem solar cell, scanned from forward to reverse bias (Reverse) and from reverse to forward bias (Forward) at a scan rate of 100 mV/s. Inset: the all-perovskite tandem device stack,*[34] *b) maximum power point tracking (top, black line) and* V_{oc} *tracking (bottom, red line) of an all-perovskite tandem solar cell.*

Table 1: *Performance parameters of all-perovskite tandems (average of 28 devices), and the champion device.*

	V_{OC} (V)	J_{SC} (mA/cm^2)	FF (%)	Rev PCE (%)	Fwd PCE (%)
Average	1.95 ± 0.03	15.3 ± 0.4	75.0 ± 1.5	22.3 ± 0.7	21.9 ± 0.6

Champion	2.05	15.6	74.8	23.8	23.3

EIS measurements were performed at open-circuit potential (V_{OC}) under illumination, using a potentiostatic excitation applied at logarithmically distributed frequencies between 10^{-1} and 10^{6} Hz (see Methods). The V_{oc} decreases in the first minutes, but stabilises after three minutes of illumination (Figure 1b). To account for the initial drop in V_{oc}, devices are held at V_{oc} for three minutes before the measurement is started. The Nyquist (Figure 2a,b) and corresponding imaginary impedance (-Z'') *vs* frequency plots (Figure 2d,e) for wide gap and narrow gap SJ perovskite devices show two clear semicircles and two distinct peaks, respectively. For PSCs, the high frequency RC time constant is related to non-radiative recombination and the geometric capacitance of the device. Note that radiative recombination is too fast to be probed with EIS. The origin of the low frequency time constant is still debated, but a consensus is beginning to emerge that the low frequency response is caused by the ion modulated recombination current.[25,35] In this work we limit ourselves to denominating the high frequency semicircle as the electronic recombination time constant, relating to the recombination resistance (but note that this does not encompass radiative recombination) and geometric capacitance and the low frequency semicircle as the ionic RC time constant, relating to ionic modulation of the recombination (or injection) current. These denominations are used for simplicity, though the true nature of the electronic and ionic processes is complex and discussed in detail elsewhere.[26,29,30,36,37] Characteristic relaxation time constants for these processes can be expressed in terms of resistance (R) and capacitance (C), although extreme care has to be taken when assigning physical meaning to these parameters.[25] Relaxation processes can be modelled with a resistor-capacitor equivalent circuit (EC), from which the relaxation time constant τ can be found:

$$\tau = RC$$

Note, however, that for PSCs the capacitor element is often replaced by a constant phase element (CPE) to account for sample inhomogeneity.[25] Alternatively, τ can be derived from the apex frequency (f) of –Z'':

$$\tau = 1/(2\pi f)$$

Both methods should return identical values for τ. Throughout this paper we denote the time constant for the high frequency arc the 'electronic recombination time constant'. The time constants for all lower frequency processes are denoted 'ionic time constants' as they occur on timescales where ionic motion modulates the current measured from the devices. It is important to note that these characteristic time constants are indicative of processes occurring in the cell, but do not directly give electron lifetimes. It is also important that time constant and lifetime are not used interchangeably. Electronic recombination and ionic time constants can be readily extracted for these SJ devices by either EC fitting, using a series resistance element and two R-CPE elements in series (Figure S2a), hereafter referred to as SJ EC, or from the frequency corresponding to the apex of the Nyquist plot. Here, we will focus on the value extracted from EC fitting, as it provides a more detailed analysis, and use the apex frequency to verify the validity of the time constant found. Electronic recombination and ionic time constants for the devices in Figure 2 can be found in Table 2. The corresponding resistance and capacitance values are listed in Table S2. The frequency of the apex of the Nyquist plot can be displayed by plotting –Z'' *vs* frequency, allowing shifts in time constants to be elegantly visualised.

Typical Nyquist and -Z'' *vs* frequency plots for an all-perovskite tandem device are shown in Figure 2c and f, respectively. There are two distinct low frequency semicircles, although we note that this is not always the case (Figure S3). The high frequency signals for both sub-cells heavily overlap, making it difficult to extract time constants for individual processes, and is indeed impossible using the apex frequency approach. An EC consisting of a series resistance and four R-CPE elements (Figure S2b, hereafter referred to as tandem EC) can be rationalised by assuming that each sub-cell will have its own electronic recombination and ionic time constants. However, this approach has two major shortcomings. First, in spectra where semicircles overlap significantly, it is impossible to find a satisfactory fit for the individual relaxation time constants (HF semicircle in Figure 2c), as we have to guess where one feature ends and the next one starts. Secondly, even if two distinct relaxation time constants can be observed, it is not obvious which relaxation time constant belongs to which sub-cell, therefore making it difficult to identify performance limiting bottlenecks.

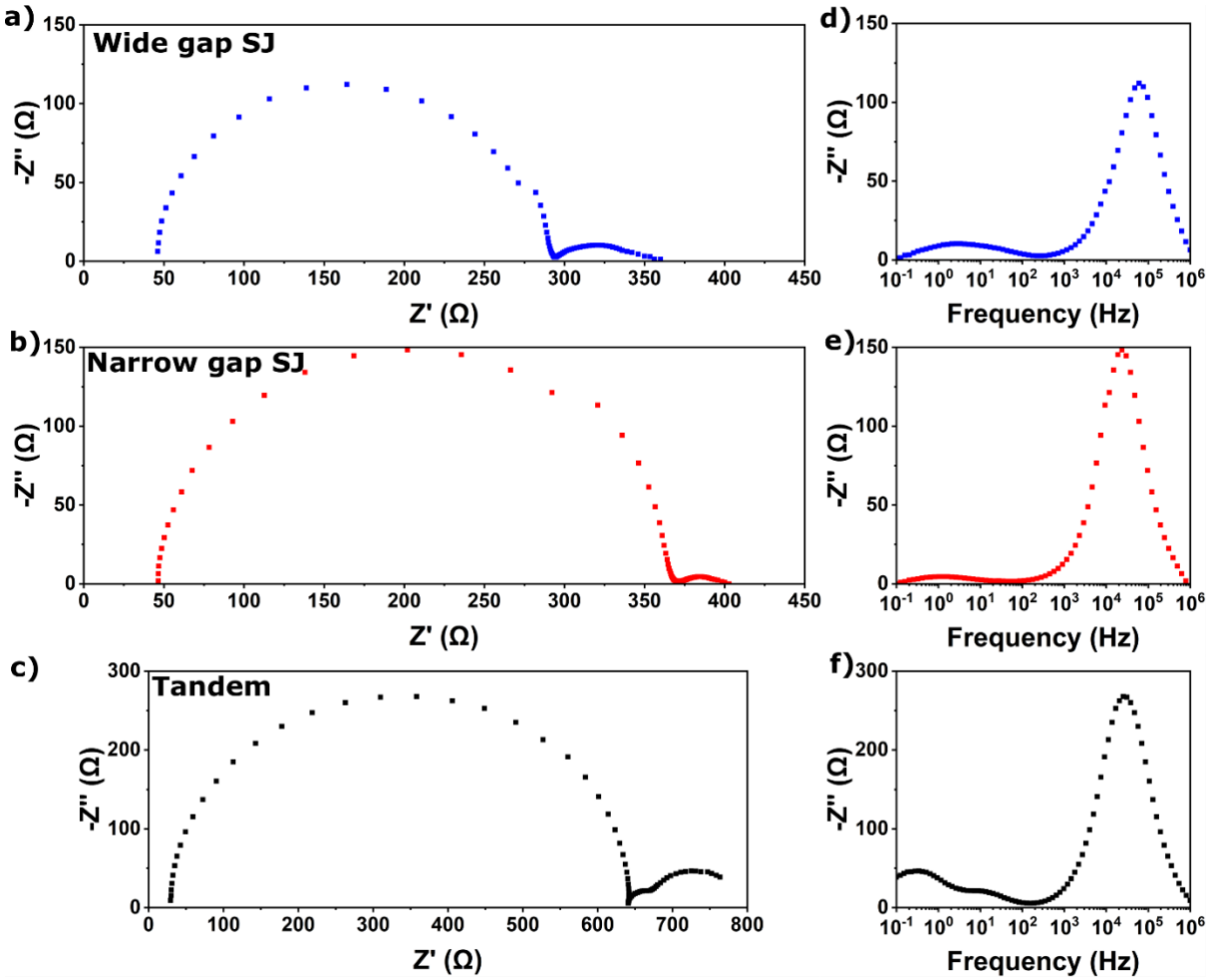

Figure 2: *Nyquist plots of a) wide gap SJ, b) narrow gap SJ and c) all-perovskite tandem solar cells (see Table 1 and Table S1 for corresponding device parameters). -Z''* vs *frequency plots of d) wide gap SJ, e) narrow gap SJ and f) all-perovskite tandem solar cells. Devices were illuminated using full spectrum AM1.5G illumination at 0.1 sun intensity and measured at* V_{oc}*, with a wait time of three minutes before each measurement to allow* V_{oc} *to stabilise. Note the different scales of the x-axis in a-c.*

Table 2: *Relaxation time constants for electronic recombination and ionic processes for the SJs and tandem in Figure 2. Corresponding resistances, capacitances and apex frequencies can be found in Table S2.*

Device	Process	R (Ω)	CPE (F)	τ (s)
Wide gap SJ	Recombination	237	$1.09*10^{-8}$	**2.6×10^{-6}**
	Ionic	62.0	$9.29*10^{-4}$	**5.8×10^{-2}**
Narrow gap SJ	Recombination	320	$2.12*10^{-4}$	**6.8×10^{-6}**
	Ionic	24.9	$5.40*10^{-3}$	**1.3×10^{-1}**
Tandem	Recombination	629	$9.06*10^{-9}$	**5.7×10^{-6}**
	Ionic	19.4	$2.79*10^{-4}$	**5.4×10^{-3}**
		144	$4.70*10^{-3}$	**6.8×10^{-1}**

To further understand the EIS signal of the tandem, we first explored the influence of the illumination intensity on the EIS signal of the equivalent SJ devices. Wide gap and narrow gap SJ devices were illuminated using full spectrum AM1.5G light, with intensity ranging from 1.0 to 0.01 sun, while performing EIS measurements. The corresponding Nyquist and -Z'' *vs* frequency plots are displayed in Figure S4 (corresponding relaxation time constants are in Table S3). It can clearly be seen in the Nyquist plots that both *Z'* and *–Z''* increase with decreasing light intensity. An intrinsic factor contributing to this increase is that the rate of carrier generation decreases with decreasing light intensity (Figure S5). As the measurement is performed at open circuit, this means the rate of recombination also decreases. The recombination current is inversely proportional to the recombination resistance, hence as the current decreases the recombination resistance increases and the diameter of the high frequency arc in the Nyquist plot increases.[25] Further to this, carrier lifetime generally increases with decreasing light intensity,[38] resulting in increased impedance. Additionally, the apex frequencies of all semicircles show distinct shifts (Figure S4, Table S3).

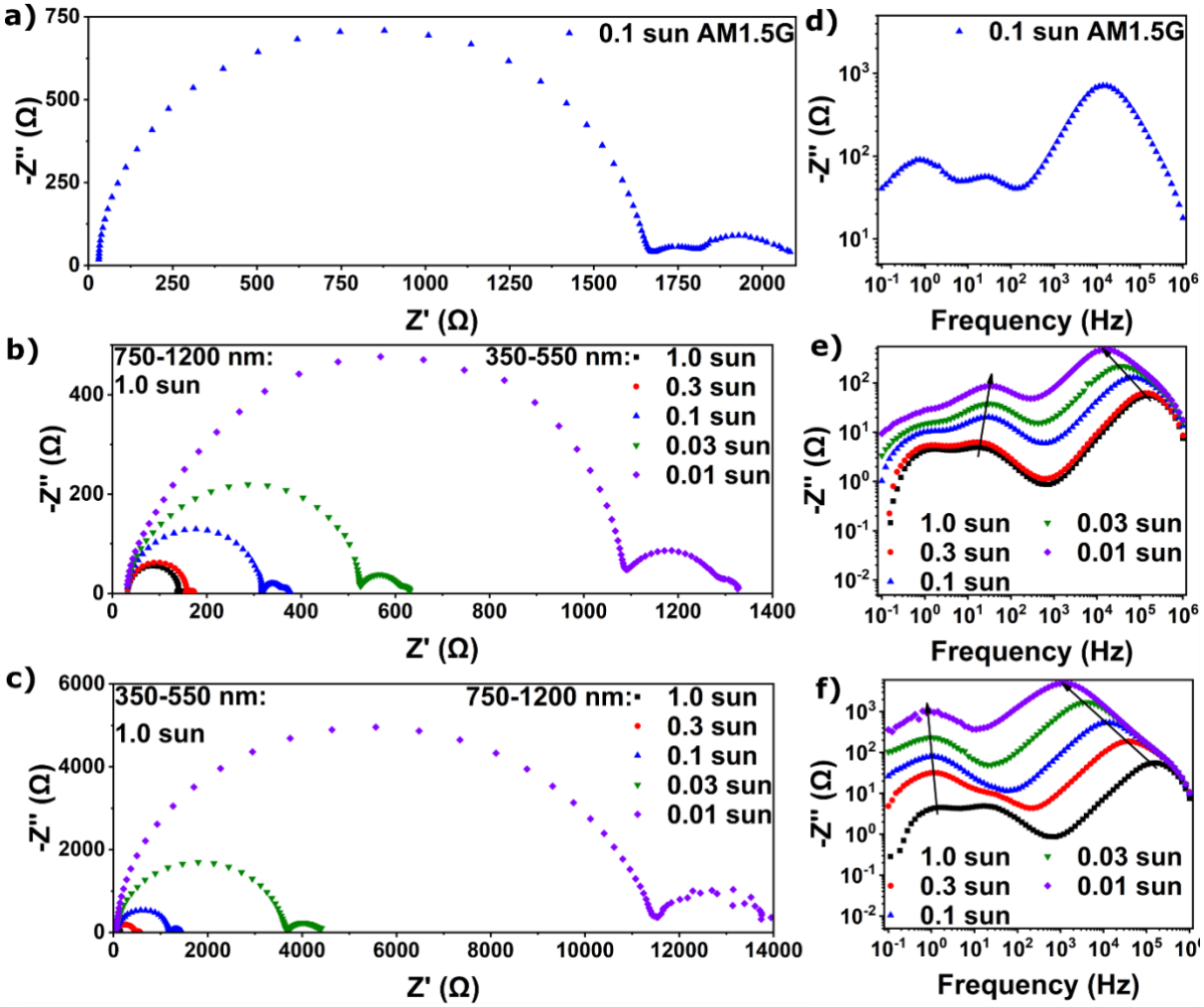

Figure 3: *Nyquist plots of an all-perovskite tandem solar cell a) with 0.1 sun full spectrum AM1.5G illumination, b) with 1.0 sun 750-1200 nm light and varying 350-550 nm light, allowing the wide bandgap sub-cell to be studied, and c) with 1.0 sun 350-550 nm light and varying 750-1200 nm light, allowing the narrow bandgap sub-cell to be studied. -Z''* vs *frequency plots of an all-perovskite tandem solar cell d) with 0.1 sun full spectrum AM1.5G illumination, e) with 1.0 sun 750-1200 nm light and varying 350-550 nm light and f) with 1.0 sun 350-550 nm light and varying 750-1200 nm light. Devices were measured at* V_{oc}*, with a wait time of three minutes before each measurement to allow* V_{oc} *to stabilise. Note the different scales of the x-axis in a-c.*

The illumination intensity can thus be used to manipulate the magnitude and characteristic frequency of the EIS signal. Each sub-cell in the tandem device absorbs a range of wavelengths which the other sub-cell does not absorb (Figure S1). This allows us to magnify the signal from one of the sub-cells, while suppressing the signal from the other sub-cell, and allow sub-cell selective measurements. The Nyquist and -Z'' *vs* frequency plots at 0.1 sun full spectrum AM1.5G illumination of an all-perovskite tandem are shown in Figure 3a and Figure 3d (relaxation time constants can be found in Table S4). An LED solar simulator was used to achieve spectral control, where the intensity of 22 different wavelengths in the wavelength range of 350-1200 nm can be individually set. To selectively characterise the wide gap sub-cell, the narrow gap sub-cell signal was suppressed by using 1 sun intensity illumination in the 750-1200 nm range, which is only absorbed by the narrow gap sub-cell. The intensity of the 350-550 nm range, which is primarily absorbed by the wide gap sub-cell (Figure

S1), was dialled down from 1 sun to 0.01 sun intensity to amplify the wide gap sub-cell signal, and study how the EIS signal changes over this intensity range (Figure 3b,e). To study the narrow gap sub-cell, the intensity of the 350-550 nm range was set to 1 sun, while the 750-1200 nm range was dialled down from 1 sun to 0.01 sun (Figure 3c,f). The 550-750 nm range was not used here, as it is absorbed by both sub-cells. Note that sun intensity refers to the intensity the specific wavelength ranges have in the AM1.5G spectrum; see Figure S6 for irradiance data of all spectra used. We note that because the 550-750 nm range in which both sub-cells absorb is omitted, the total irradiance of each sub-cell is lower than for the AM1.5G illumination used for SJs (Figure S4, Table S3), and care should be taken when comparing the results from SJs to sub-cells directly.

The Nyquist plots in Figure 3b and 3c illustrate again the large increase in resistance when the intensity of the illumination is reduced from 1.0 to 0.01 sun, with the exception that the contribution of the sub-cell illuminated at 1.0 sun should stay the same, and that the increase in signal is dominated by the signal originating from the sub-cell of interest. The -Z'' *vs* frequency plots in Figure 3e and 3f also show that the contribution of the sub-cell illuminated at 1.0 sun stays constant, whereas the signal of the sub-cell of interest increases and displays a shift in the apex frequency. It is now possible to extract the relaxation time constants by fitting the Nyquist plots with the SJ EC, or by using the apex frequency of the -Z'' *vs* frequency plots (Table S5). Relaxation time constants are on the same order of magnitude as those found for the corresponding SJ devices (Table S3, Figure S7), validating the selective illumination method. Note however, that the illumination spectra and intensities used here are different for single junctions and for their tandem sub-cell counterparts. For a quantitative comparison between single junctions and their tandem sub-cell counterparts, the incident illumination spectra have to be matched precisely, to ensure carrier densities are the same for both devices. For both EC fitting and apex frequency, full spectrum illumination (Figure 3d) gives accurate ionic relaxation time constants, but only one electronic recombination relaxation time constant (which happens to match well with the narrow gap sub-cell). On the other hand, using selective illumination (Figure 3e and f) gives relaxation time constants that match well between EC fitting and using the apex frequency, and SJ devices (Table S3).

Overall, using the selective illumination method yields results that are more consistent with SJ devices, and between the EC fitting and apex frequency methods of finding relaxation time constants. Additionally, the approach makes it immediately clear which sub-cell the extracted relaxation time constants belong to. We emphasize that this information cannot be extracted using full spectrum AM1.5G light and the tandem EC.

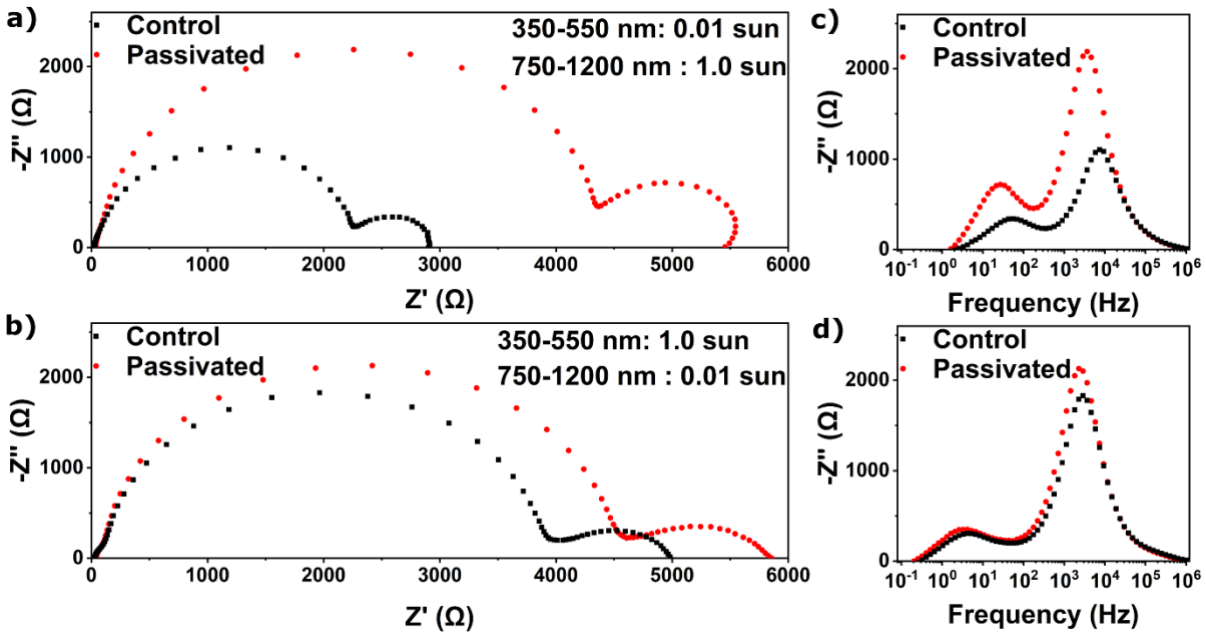

Figure 4: *Nyquist plots of a control and a wide gap passivated all-perovskite tandem solar cell a) with 0.01 sun 350-550 nm and 1.0 sun 750-1200 nm light and light, allowing the wide bandgap sub-cell to be studied, and b) with 1.0 sun 350-550 nm light and 0.01 sun 750-1200 nm light, allowing the narrow bandgap sub-cell to be studied. -Z'' vs frequency plots of an all-perovskite tandem solar cell c) with 0.01 sun 350-550 nm and 1.0 sun 750-1200 nm light and d) with 1.0 sun 350-550 nm light and 0.01 sun 750-1200 nm light. Devices were measured at* V_{oc}*, with a wait time of three minutes before each measurement to allow* V_{oc} *to stabilise.*

Table 3: *Relaxation time constants for electronic recombination and ionic processes for the control and passivated all-perovskite tandems in Figure 4. Corresponding resistances, capacitances and apex frequencies can be found in Table S8.*

Device	Sub-cell	Process	R (Ω)	CPE (F)	τ (s)
Control	Wide gap	Recombination	2160	$9.73*10^{-9}$	**2.1×10^{-5}**
		Ionic	783	$3.47*10^{-6}$	**2.7×10^{-3}**
	Narrow gap	Recombination	3880	$1.48*10^{-8}$	**5.7×10^{-5}**
		Ionic	1030	$3.28*10^{-5}$	**3.4×10^{-2}**
Passivated	Wide gap	Recombination	4290	$1.01*10^{-8}$	**4.3×10^{-5}**
		Ionic	1290	$4.66*10^{-6}$	**6.0×10^{-3}**
	Narrow gap	Recombination	4300	$1.48*10^{-8}$	**6.4×10^{-5}**
		Ionic	1310	$3.16*10^{-5}$	**4.1×10^{-2}**

We now use the selective illumination method to study the effect of passivating the wide gap sub-cell on electronic recombination and ionic motion in both the wide gap and narrow gap sub-cells of an all-perovskite tandem solar cell (Figure 4). $PDAI_2$ was used as passivating agent, which was found to increase all performance parameters of bromide-rich SJ perovskite solar cells (Table S6).[17] EIS analysis of SJs (Figure S8, Table S7) shows that passivation increases the electronic recombination resistance ~1.7 times (from 3240 Ω to 5370 Ω) and the electronic recombination time constant ~1.5 times (from 42 µs to 60 µs). The ionic time constant increases ~1.6 times (from 1.3 ms to 2.1 ms). These findings are in agreement with reports that passivation reduces the number of mobile defects and non-

radiative recombination, leading to improved device performance.[17] PL mapping of wide gap SJs shows an increase in PL intensity by a factor of ~5, confirming that $PDAI_2$ passivation reduces the density of defect states (Figure S9). For the all-perovskite tandem, using full spectrum AM1.5G illumination for EIS does not yield any useful information (Figure S10). However, the selective illumination method clearly shows that electronic recombination resistance and time constant, and ionic time constants for the wide gap sub-cell have increased significantly (Figure 4a,c, Table 3, Table S8). The electronic recombination resistance and time constant increase ~2.0 times (from 2160 Ω to 4290 Ω and from 21 µs to 43 µs, respectively) and the ionic time constant increases ~2.2 times (from 2.7 ms to 6.0 ms), showing that $PDAI_2$ passivation effectively improves the performance of wide gap sub-cells in all-perovskite tandems as well. We showed that time constants decrease with increasing V_{oc} (Table S3, Figure S5). The V_{oc} of passivated devices is ~40 mV higher than the V_{oc} of control devices, which should decrease the time constants of passivated devices compared to control devices. This makes the fact that the time constants have actually increased even more significant. These results are again supported by a PL intensity increase by a factor of ~3 for the passivated wide gap sub-cell, compared to the control wide gap sub-cell (Figure S10). The electronic recombination resistance and time constant of the narrow gap sub-cell increase ~1.1 times (from 3880 Ω to 4300 Ω and from 57 µs to 64 µs, respectively), and the ionic motion time constant increases ~1.2 times (from 34 ms to 41 ms). $PDAI_2$ influences the number and time constant of charge carriers transported from the wide gap perovskite to the recombination junction.[17,39] $PDAI_2$ passivation of the wide gap sub-cell will thus also affect electronic and ionic processes at the interface between the recombination junction and the narrow gap sub-cell by determining how many charge carriers are available for recombination and ionic processes.[35] Examples of ionic processes that depend on the availability of electronic charge carriers are the photolysis of PbI_2[40] and the (de)doping of Sn-based perovskites,[41] whereas ion-modulated recombination is an example of a process where the availability of ions influences the electronic recombination lifetime. Increased time constants in the narrow gap sub-cell indicate that charges take longer to reach the recombination layer, potentially because $PDAI_2$ forms a charge extraction barrier in the wide gap sub-cell; further work beyond the scope of this current work would be needed to explore this further. In addition to tracking improvements of individual sub-cells in the tandem stack as we have done here, the selective illumination method could also be used as quality control, pinpointing problems in batches that perform below the baseline to a specific sub-cell.

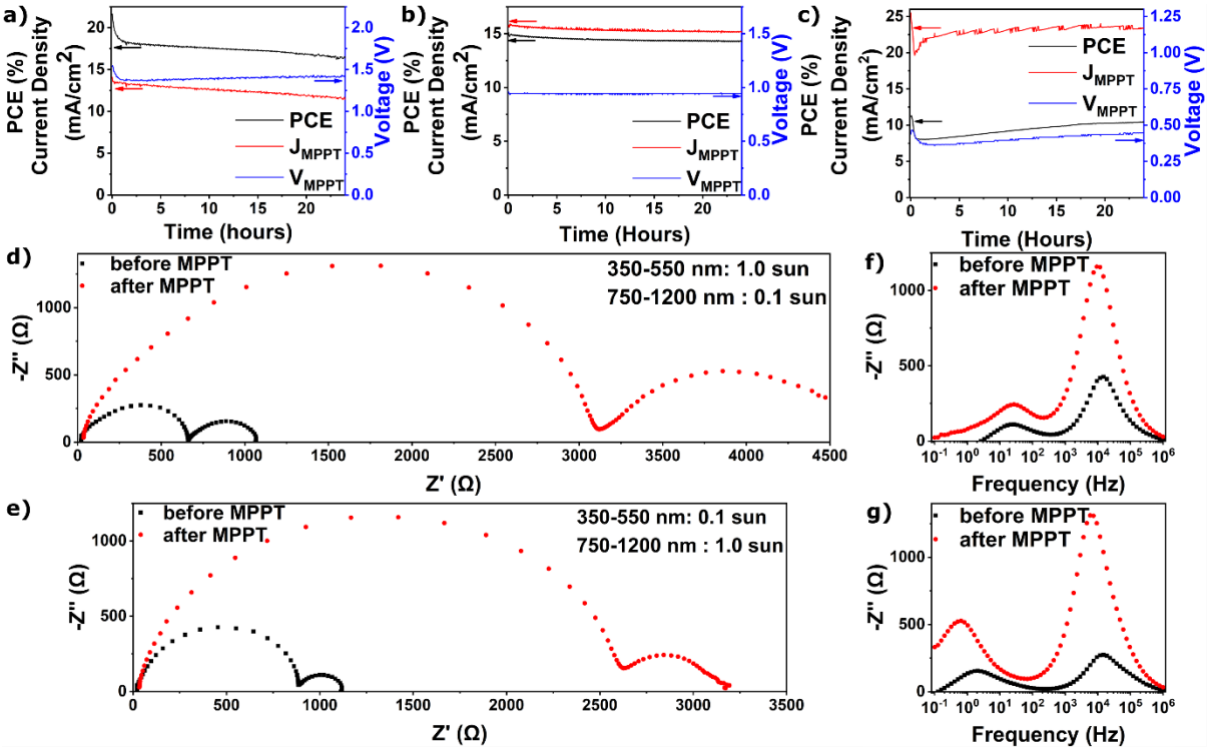

Figure 5: *Maximum power point tracking of a) an all-perovskite tandem solar cell, b) wide gap SJ, c) narrow gap SJ solar cell, showing power conversion efficiency (PCE) during tracking and corresponding current density (J_{MPPT}) and voltage (V_{MPPT}). The devices were encapsulated with 25 nm of SnO_x deposited by atomic layer deposition, and measured in ambient air under 1.0 sun intensity AM1.5G illumination. Nyquist plots of an all-perovskite tandem solar cell before and after maximum power tracking for 24 hours, d) with 0.1 sun 350-550 nm and 1.0 sun 750-1200 nm light and light, allowing the wide bandgap sub-cell to be studied, and e) with 1.0 sun 350-550 nm light and 0.1 sun 750-1200 nm light, allowing the narrow bandgap sub-cell to be studied. -Z'' vs frequency plots of an all-perovskite tandem solar cell f) with 0.1 sun 350-550 nm and 1.0 sun 750-1200 nm light and g) with 1.0 sun 350-550 nm light and 0.1 sun 750-1200 nm light. Devices were measured at V_{oc}, with a wait time of three minutes before each measurement to allow V_{oc} to stabilise.*

Table 4: *Relaxation time constants for electronic recombination and ionic processes before and after MPPT for the all-perovskite tandem in Figure 5. Corresponding resistances, capacitances and apex frequencies can be found in Table S9.*

Device	Sub-cell	Process	R (Ω)	CPE (F)	τ (s)
Before MPPT	Wide gap	Recombination	836	$1.34*10^{-8}$	**1.1×10^{-5}**
		Ionic	240	$2.49*10^{-5}$	**6.0×10^{-3}**
	Narrow gap	Recombination	560	$1.95*10^{-8}$	**1.1×10^{-5}**
		Ionic	386	$2.02*10^{-4}$	**7.8×10^{-2}**
After MPPT	Wide gap	Recombination	2580	$6.06*10^{-9}$	**1.6×10^{-5}**
		Ionic	488	$1.21*10^{-5}$	**5.9×10^{-3}**
	Narrow gap	Recombination	2810	$8.53*10^{-9}$	**2.4×10^{-5}**
		Ionic	1450	$1.81*10^{-4}$	**2.6×10^{-1}**

To explore if EIS can be used to study degradation of all-perovskite tandem solar cells, we subjected an all-perovskite tandem solar cell to 24 hours of maximum power point tracking (MPPT) under illumination, during which the tandem degraded to ~75% of its initial efficiency (Figure 5a). We observe a fast drop in PCE in the first hour of MPPT driven by a decrease in voltage, followed by a slower decay driven by decreasing current density. The MPPT traces of equivalent wide gap SJ devices only show a small initial decrease in both voltage and current (Figure 5b). Equivalent narrow gap SJ devices show a fast drop in efficiency in the first hour, followed by a slow increase, mainly driven by changes in voltage (Figure 5c). It is important to note that V_{oc} of the devices does not decrease under MPPT conditions (Table S10). However, this does not mean that the underlying physical processes that determine V_{oc} have not changed; in fact our results indicate that these processes have changed, but their net influence on V_{oc} is close to zero. The slower decay driven by decreasing current density that was observed for the tandem is absent for both SJ devices. To gain more insight as to why the tandem degrades differently than the corresponding individual SJ devices, we performed EIS using selective illumination. Full spectrum illumination clearly shows changes in electronic recombination and ionic time constants, but does not provide sub-cell specific information (Figure S12). Selective illumination allows us to see what is happening in each sub-cell when the tandem is subjected to MPPT measurements (Figure 5d-g). Surprisingly, the electronic recombination resistance for both sub-cells has increased significantly following degradation, ~3.1 times (from 836 Ω to 2580 Ω) for the wide gap sub-cell and ~5.0 times (from 560 Ω to 2810 Ω) for the narrow gap sub-cell. The geometric capacitance on the other hand decreases ~2.2 times (from 13.4 nF to 6.06 nF) for the wide gap sub-cell and ~2.3 times (from 19.5 nF to 8.53 nF) for the narrow gap sub-cell. This results in an increase of the recombination time constant by ~1.5 times (from 11 µs to 16 µs) for the wide gap sub-cell and ~2.2 times (from 11 µs to 24 µs) for the narrow gap sub-cell (Table 4). At the same time, PL mapping shows that PL intensity decreases ~2 times for the wide gap sub-cell (Figure S11), whereas the PL intensity increases ~10 times for the narrow gap sub-cell (Figure S13). The PL increase for the narrow gap sub-cell after MPPT is surprising, but was found repeatedly in different device batches (Figure S13). Note that Sn-based perovskites need higher illumination intensities for reliable PL measurements (6-10 suns), but due to the relatively short measurement time compared to the 24-hour stability test, it is not expected that the PL measurement induces additional changes. Interestingly, EIS shows here that overall non-radiative recombination decreases, while PL shows that radiative recombination decreases for the wide gap sub-cell, but increases for the narrow gap sub-cell. The decreased geometric capacitance indicates a reduction in surface roughness[42] or the formation of materials with lower dielectric constants.[24] These results could potentially be caused by changes in the perovskite absorber materials, as well as by the formation of an interfacial charge extraction barrier.

To investigate further, we performed UV/Vis absorption (Figure S14) on all-perovskite tandems before and after 24 hours of MPPT. Despite a ~20% drop in current density, there is no appreciable drop in absorption, indicating that the perovskite materials are still absorbing the same amount of light and that charge transport and extraction may be limiting the obtainable current density. EQE (Figure S15) measurements show that for both sub-cells current density decreases by ~15% after the MPPT procedure. The observation that current decreases equally for both sub-cells, points towards the recombination layer or the sub-cell/recombination layer interface as the origin of the decreasing current. The recombination layer electrically connects the two sub-cells. Its main functions are to provide a solvent barrier to protect the wide gap top cell during processing of subsequent layers, and to facilitate efficient recombination between electrons from the wide gap sub-cell and holes from the

narrow gap sub-cell. In our tandem stack, SnO_x serves as solvent barrier and a 1 nm Au layer facilitates recombination (inset Figure 1a). Au is known to migrate under electrical bias,[43] which could lead to a gradual decline of the recombination facilitating qualities of the recombination layer. Alternatively, a charge extraction barrier could form at the sub-cell/recombination layer interface. A charge extraction barrier at the Au/HTM interface, for example through the formation of gold-iodide complexes,[44] or electrochemical oxidation of Sn,[45] could explain the recombination dynamics found by EIS and PL. If an extraction barrier is formed at the narrow gap sub-cell/recombination layer interface during the MPPT procedure, charges generated in the wide gap sub-cell can still easily travel to the Au recombination junction, where recombination is limited by the availability of charges from the narrow gap sub-cell, which have to overcome the newly formed charge extraction barrier before recombining, prolonging the electronic lifetime for charges from the wide gap sub-cell, without increasing radiative recombination in the wide gap sub-cell, as the charges in the recombination junction cannot recombine radiatively. Further evidence for this hypothesis is that the electronic and ionic lifetimes of a wide gap single junction device do not significantly change after MPPT (Figure S16, Table S11), indicating that the observed changes in the tandem stack are likely related to the recombination junction. Meanwhile, in the narrow gap sub-cell, charges are extracted slower as a result of the charge extraction barrier, leading to reduced quenching of the radiative component, explaining the increased PL. This hypothesis can explain the increased (non-radiative) recombination time constant in both sub-cells. The observations that the (non-radiative) recombination time constant increases less for the wide gap sub-cell than for the narrow gap sub-cell, and that radiative recombination (from PL) decreases in the wide gap sub-cell, indicate that some degradation takes place in the wide gap sub-cell. Further confirmation that a charge extraction barrier is formed in the narrow gap sub-cell, is the three times increased ionic time constant for the narrow gap sub-cell, whereas the ionic time constant for the wide gap sub-cell remains the same. This indicates that the narrow gap sub-cell has undergone chemical changes, whereas this is not the case for the wide gap sub-cell, providing further evidence that an extraction barrier is formed in the narrow gap sub-cell. We show here that EIS can provide crucial insights into non-radiative recombination and ionic processes. In combination with other characterisation techniques, EIS can offer a comprehensive picture of processes happening in perovskite solar cells, help to identify potential bottlenecks, and improve efficiency and stability of these devices,

EIS is a powerful technique to study processes such as electronic recombination and ionic processes in devices under operating conditions. The EIS signal of all-perovskite tandems is much more complex than that of SJ perovskite devices, with overlapping signals complicating the physical interpretation. In many cases EC modelling does not give satisfactory values for the modelled parameters. Even in the cases where modelling does work, it is not obvious to which sub-cell each parameter belongs. Illumination intensity can strongly modulate the EIS signal, and it is shown that for both wide gap and narrow gap perovskite SJs the apex frequency significantly shifts, and the impedance can be reduced by several orders of magnitude by increasing illumination intensity. This can be exploited by making use of the absorption properties of the individual sub-cells in the tandem stack. The wide gap sub-cell selectively absorbs wavelengths <550 nm, thus selective illumination (1.0 sun intensity) with 350-550 nm light suppresses the signal from the wide gap sub-cell and allows the selective measurement of the narrow gap sub-cell. Similarly, the narrow gap sub-cell selectively absorbs wavelengths >750 nm. Using this methodology, electronic recombination and ionic relaxation time constants can be extracted and assigned to individual sub-cells. Using the selective illumination method, we show that

$PDAI_2$ passivation increases the performance of wide gap sub-cells, similar to wide gap SJs. In addition, we find that during MPPT a charge transport barrier is formed at the recombination layer/narrow gap sub-cell interface, indicating that replacing Au in the recombination layer with other conductive materials could improve the stability of all-perovskite tandems. We demonstrate the versatility of the selective illumination EIS method to better understand all-perovskite tandems. In combination with other advanced characterization techniques, such as elemental mapping and transient lifetime measurements, EIS will be a powerful tool to understand recombination and degradation processes in all-perovskite tandem solar cells. An enhanced understanding of how all-perovskite tandems operate will allow targeted methods to address bottlenecks and ultimately allow these devices to achieve their full potential. The method can also be applied to other tandem solar cell technologies, such as silicon/perovskite tandems, to better understand these devices.

Perovskite solution preparation

$Cs_{0.25}FA_{0.75}Pb(I_{0.767}Br_{0.233})$: A 0.85M solution of $Cs_{0.25}FA_{0.75}Pb(I_{0.767}Br_{0.233})$ was prepared by dissolving 0.6375M formamidinium iodide (FAI, Greatcell Solar), 0.2125M cesium iodide (CsI, Sigma-Aldrich), 0.3825M lead bromide (TCI) and 0.476M lead iodide (PbI_2, TCI) in a 4:1 (vol:vol) mixture of N,N-dimethylformamide (DMF, Sigma-Aldrich) and dimethylsulfoxide (DMSO, Sigma-Aldrich). The solution was stirred at 50°C for 2 hours and filtered using a 0.22 µm PTFE membrane before use.

$Cs_{0.15}FA_{0.85}Pb_{0.5}Sn_{0.5}I_3$: A 1.35M solution of $Cs_{0.15}FA_{0.85}Pb_{0.5}Sn_{0.5}I_3$ was prepared by dissolving 1.1475M FAI, 0.2025M CsI, 0.675M PbI_2, 0.675M SnI_2 and 0.0675M SnF_2 in a 3:1 (vol:vol) mixture of DMF/DMSO. The solution was stirred for 2 hours and filtered using a 0.22 µm PTFE membrane before use.

Wide gap SJ fabrication

Patterned ITO glass substrate (KINTEC Company) were cleaned using 15 minutes of sonication in a 2% Hellmanex III (Sigma-Aldrich) solution, followed by 5 minutes in DI water, 15 minutes in acetone and 15 minutes in isopropanol. The substrates were dried using a nitrogen stream and subjected to a 15 minute UV/Ozone treatment before being transferred into a nitrogen-filled glovebox. A 1 mM solution of 2PACz in anhydrous ethanol was spincoated at 3000 rpm (5s ramp) for 30s, followed by annealing for 10 minutes at 100°C. After cooling down to room temperature, $Cs_{0.25}FA_{0.75}Pb(I_{0.767}Br_{0.233})$ perovskite was deposited onto the substrates by spincoating at 2000 rpm for 10s (2s ramp) and 6000 rpm for 40s (4s ramp). Anhydrous chlorobenzene was dripped onto the spinning substrate 20s before the end of the program. The substrates were then annealed for 30 minutes at 100°C.[14] A 0.25mg/ml solution of $PDAI_2$ (Sigma-Aldrich) in a 1:1 (vol:vol) mixture of isopropanol and toluene was stirred overnight at 50°C, filtered using a 0.22 µm PTFE membrane and subsequently spincoated at 4000 rpm for 20s, followed by annealing at 100°C for 5 minutes.[17] The substrates were then transferred to a thermal evaporator for deposition of 20nm of C60 (Sigma-Aldrich), 7nm of bathocuproine (Sigma-Aldrich) and 120 nm of Cu.

Narrow gap SJ fabrication

Patterned ITO glass substrate (KINTEC Company) were cleaned using 15 minutes of sonication in a 2% Hellmanex III (Sigma-Aldrich) solution, followed by 5 minutes in DI water, 15 minutes in acetone and 15 minutes in isopropanol. The substrates were dried using a nitrogen stream and subjected to a 15 minute UV/Ozone treatment. A filtered (0.45 µm membrane) 3:1 solution of methanol (Sigma-Aldrich) and PEDOT:PSS (Clevios Heraeus Al 4083) was spincoated on top of the substrates at 4000 rpm (3.5s ramp) for 30s, followed by annealing at 140°C for 20 minutes. After removing the substrates from the

hotplate, they were immediately transferred to a nitrogen filled glovebox. $Cs_{0.15}FA_{0.85}Pb_{0.5}Sn_{0.5}I_3$ was spincoated at 5000 rpm (4s ramp) for 50s. Anisole was dripped onto the spinning substrate 25s before the end of the program. The substrate was immediately transferred to a hotplate and annealed at 100°C for 10 minutes. A 0.5mg/ml solution of $EDAI_2$ (Sigma-Aldrich) in a 1:1 (vol:vol) mixture of isopropanol and toluene was stirred for overnight at 50°C, filtered using a 0.22 µm PTFE membrane and subsequently spincoated at 4000 rpm for 20s, followed by annealing at 100°C for 5 minutes.[46] After cooling down to room temperature, 20nm of C60, 7nm of bathocuproine (Sigma-Aldrich) and 120 nm of Cu were deposited by thermal evaporation.

All-perovskite tandem fabrication

Patterned ITO glass substrate (KINTEC Company) were cleaned using 15 minutes of sonication in a 2% Hellmanex III (Sigma-Aldrich) solution, followed by 5 minutes in DI water, 15 minutes in acetone and 15 minutes in isopropanol. The substrates were dried using a nitrogen stream and subjected to a 15 minute UV/Ozone treatment before being transferred into a nitrogen-filled glovebox. A 1mM solution of 2PACz in anhydrous ethanol was spincoated at 3000 rpm (5s ramp) for 30s, followed by annealing for 10 minutes at 100°C. After cooling down to room temperature, $Cs_{0.25}FA_{0.75}PbI_{2.1}Br_{0.9}$ perovskite was deposited onto the substrates by spincoating at 2000 rpm for 10s (2s ramp) and 6000 rpm for 40s (4s ramp). Anhydrous chlorobenzene was dripped onto the spinning substrate 20s before the end of the program. The substrates were then annealed for 30 minutes at 100°C. A 0.25mg/ml solution of $PDAI_2$ (Sigma-Aldrich) in a 1:1 (vol:vol) mixture of isopropanol and toluene was stirred overnight at 50°C, filtered using a 0.22 µm PTFE membrane and subsequently spincoated at 4000 rpm for 20s, followed by annealing at 100°C for 5 minutes.[17] The substrates were then transferred to a thermal evaporator for deposition of 20nm of C60 (Sigma-Aldrich). A 25nm SnO_2 interlayer was deposited by atomic layer deposition (Picosun). Tetrakis(dimethylamino)tin(IV) (TDMASn, EpiValence) was used as precursor and H_2O as reactant. The precursor bubbler was heated to 75°C and the chamber to 100°C, the reactant vessel was kept at room temperature. The pulsing sequence consisted of a 0.6s pulse of TDMASn, 30s purge, 0.1s pulse of H_2O, 30 s purge, resulting in a growth rate of 0.1 nm/cycle. Following ALD, 1 nm of Au was deposited by thermal evaporation. The substrates were removed from the glovebox and a filtered (0.45 µm membrane) 3:1 solution of methanol (Sigma-Aldrich) and PEDOT:PSS (Clevios Heraeus Al 4083) was subsequently spincoated on top of the substrates at 4000 rpm (3.5s ramp) for 30s, followed by annealing at 140°C for 20 minutes. After removing the substrates from the hotplate, they were immediately transferred to a nitrogen filled glovebox. $Cs_{0.15}FA_{0.85}Pb_{0.5}Sn_{0.5}I_3$ was spincoated at 5000 rpm (4s ramp) for 50s. Anisole was dripped onto the spinning substrate 25s before the end of the program. The substrate was immediately transferred to a hotplate and annealed at 100°C for 10 minutes. A 0.5mg/ml solution of ethane-1,2-diammonium iodide (Sigma-Aldrich) in a 1:1 (vol:vol) mixture of isopropanol and toluene was stirred for overnight at 50°C, filtered using a 0.22 µm PTFE membrane and subsequently spincoated at 4000 rpm for 20s, followed by annealing at 100°C for 5 minutes.[46] After cooling down to room temperature, 20nm of C60, 8nm of bathocuproine (Sigma-Aldrich) and 120 nm of Cu were deposited by thermal evaporation. For stability tests, 25 nm of SnO_2 was deposited by ALD on top of C60, followed by 120 nm of Cu.

Solar cell characterisation

Current-voltage characteristics were collected using an Arkeo multichannel platform (Cicci Research) and an LED solar simulator (G2V Sunbrick Base-UV). An aperture mask with an area of 0.1 cm^2 was used to define the active area. Devices were scanned at a scan speed of 100 mV/s. EQE and UV/Vis

absorption were measured using a Bentham PVE300 system in transformer mode. A dual xenon short-arc lamp and a quartz halogen lamp were utilized as the light source, with a swingaway mirror set to 700 nm. A 10 × 10 mm Si reference cell was used to calibrate the power of the probe beam.

Electrochemical impedance spectroscopy

EIS was performed using a Metrohm PGSTAT302N Autolab. Measurements were performed at V_{oc} and each device was allowed to equilibrate at V_{oc} for 3 minutes before each measurement. Spectra were recorded at a frequency range of 1 MHz to 0.1Hz, with an integration time of 2s and a perturbation of 40 mV. Spectra were fitted using Nova 1.12 software, employing the SJ and tandem ECs.

Photoluminescence mapping

A Photon etc. IMA system was used to carry out wide-field hyperspectral microscopy measurements. A 405-nm continuous wave laser was used for luminescence excitation. The emitted light from the sample was incident onto a volume Bragg grating, which spectrally split the light onto a temperature-controlled CCD camera operating with an operational wavelength of 400-1,000 nm. The camera was maintained at 0 °C using a thermoelectric cooler. By scanning the angle of the grating relative to the incident light, the spectral information from each point on the sample was obtained. For wide band gap perovskite samples, image sets were acquired within the range of 640 to 800 nm, while narrow band gap perovskite samples were imaged within the 880 to 1000 nm range. The step size for all measurements was set at 2 nm. The absolute number of photons at each point was determined using a two-step process.[47] Sun's intensity calculation was performed following previous literature.[47]

The Supporting Information is available free of charge at …

- EQE measurements; solar cell performance parameters; impedance spectroscopy spectra, equivalent circuits and time constants; illumination spectra; photoluminescence maps; UV/Vis

The authors acknowledge the EPSRC (EP/T02030X/1, EP/V027131/1) for funding. SDS acknowledges the Royal Society and Tata Group (grant no. UF150033). The work has received funding from the European Research Council under the European Union's Horizon 2020 research and innovation program (HYPERION, grant agreement no. 756962). Part of this work was undertaken using equipment facilities provided by the Henry Royce Institute, via the grant Henry Royce Institute, Cambridge Equipment: EP/P024947/1 and EP/R00661X/1, with additional funding from the "Centre for Advanced Materials for Integrated Energy Systems (CAM-IES)" (EP/P007767/1). K.D. acknowledges the support of the Cambridge Trust for the Cambridge India Ramanujan Scholarship and Cambridge Philosophical Society for the research studentship. MRF acknowledges funding from the EPSRC Centre for Doctoral Training in Connected Electronic and Photonic Systems (EP/S022139/1). Y-HC acknowledges the Taiwan Cambridge Trust and Rank Prize fund. For the purpose of open access, the authors have applied a Creative Commons Attribution (CC BY) license to any Author Accepted Manuscript version arising from this submission

(1) Kojima, A.; Teshima, K.; Shirai, Y.; Miyasaka, T. Organometal Halide Perovskites as Visible-Light Sensitizers for Photovoltaic Cells. *Journal of the American Chemical Society* **2009**, *131* (17), 6050–6051. https://doi.org/10.1021/ja809598r.

(2) https://www.nrel.gov/pv/cell-efficiency.html, National Renewable Energy Laboratory, (accessed 2023-08-08).

(3) Ma, C.; Park, N.-G. A Realistic Methodology for 30% Efficient Perovskite Solar Cells. *Chem* **2020**, *6* (6), 1254–1264. https://doi.org/10.1016/j.chempr.2020.04.013.
(4) Stranks, S. D.; Eperon, G. E.; Grancini, G.; Menelaou, C.; Alcocer, M. J. P.; Leijtens, T.; Herz, L. M.; Petrozza, A.; Snaith, H. J. Electron-Hole Diffusion Lengths Exceeding 1 Micrometer in an Organometal Trihalide Perovskite Absorber. *Science* **2013**, *342* (6156), 341–344. https://doi.org/10.1126/science.1243982.
(5) Green, M. A.; Ho-Baillie, A.; Snaith, H. J. The Emergence of Perovskite Solar Cells. *Nat Photon* **2014**, *8* (7), 506–514. https://doi.org/10.1038/nphoton.2014.134.
(6) Yang, F.; Jang, D.; Dong, L.; Qiu, S.; Distler, A.; Li, N.; Brabec, C. J.; Egelhaaf, H.-J. Upscaling Solution-Processed Perovskite Photovoltaics. *Advanced Energy Materials* **2021**, *11* (42), 2101973. https://doi.org/10.1002/aenm.202101973.
(7) Roose, B.; Tennyson, E. M.; Meheretu, G.; Kassaw, A.; Tilahun, S. A.; Allen, L.; Stranks, S. D. Local Manufacturing of Perovskite Solar Cells, a Game-Changer for Low- and Lower-Middle Income Countries? *Energy & Environmental Science* **2022**, *15*, 3571–3582. https://doi.org/10.1039/D2EE01343F.
(8) Eperon, G. E.; Hörantner, M. T.; Snaith, H. J. Metal Halide Perovskite Tandem and Multiple-Junction Photovoltaics. *Nature Reviews Chemistry* **2017**, *1*, 0095. https://doi.org/10.1038/s41570-017-0095.
(9) Rajagopal, A.; Yang, Z.; Jo, S. B.; Braly, I. L.; Liang, P.-W.; Hillhouse, H. W.; Jen, A. K.-Y. Highly Efficient Perovskite–Perovskite Tandem Solar Cells Reaching 80% of the Theoretical Limit in Photovoltage. *Advanced Materials* **2017**, *29* (34), 1702140. https://doi.org/10.1002/adma.201702140.
(10) Zhao, D.; Yu, Y.; Wang, C.; Liao, W.; Shrestha, N.; Grice, C. R.; Cimaroli, A. J.; Guan, L.; Ellingson, R. J.; Zhu, K.; Zhao, X.; Xiong, R.-G.; Yan, Y. Low-Bandgap Mixed Tin–Lead Iodide Perovskite Absorbers with Long Carrier Lifetimes for All-Perovskite Tandem Solar Cells. *Nature Energy* **2017**, *2* (4), 17018. https://doi.org/10.1038/nenergy.2017.18.
(11) Palmstrom, A. F.; Eperon, G. E.; Leijtens, T.; Prasanna, R.; Habisreutinger, S. N.; Nemeth, W.; Gaulding, E. A.; Dunfield, S. P.; Reese, M.; Nanayakkara, S.; Moot, T.; Werner, J.; Liu, J.; To, B.; Christensen, S. T.; McGehee, M. D.; van Hest, M. F. A. M.; Luther, J. M.; Berry, J. J.; Moore, D. T. Enabling Flexible All-Perovskite Tandem Solar Cells. *Joule* **2019**, *3* (9), 2193–2204. https://doi.org/10.1016/j.joule.2019.05.009.
(12) Bowman, A. R.; Lang, F.; Chiang, Y.-H.; Jiménez-Solano, A.; Frohna, K.; Eperon, G. E.; Ruggeri, E.; Abdi-Jalebi, M.; Anaya, M.; Lotsch, B. V.; Stranks, S. D. Relaxed Current Matching Requirements in Highly Luminescent Perovskite Tandem Solar Cells and Their Fundamental Efficiency Limits. *ACS Energy Lett.* **2021**, *6* (2), 612–620. https://doi.org/10.1021/acsenergylett.0c02481.
(13) Tong, J.; Song, Z.; Kim, D. H.; Chen, X.; Chen, C.; Palmstrom, A. F.; Ndione, P. F.; Reese, M. O.; Dunfield, S. P.; Reid, O. G.; Liu, J.; Zhang, F.; Harvey, S. P.; Li, Z.; Christensen, S. T.; Teeter, G.; Zhao, D.; Al-Jassim, M. M.; van Hest, M. F. A. M.; Beard, M. C.; Shaheen, S. E.; Berry, J. J.; Yan, Y.; Zhu, K. Carrier Lifetimes of >1 Ms in Sn-Pb Perovskites Enable Efficient All-Perovskite Tandem Solar Cells. *Science* **2019**, *364* (6439), 475–479. https://doi.org/10.1126/science.aav7911.
(14) Lin, R.; Xiao, K.; Qin, Z.; Han, Q.; Zhang, C.; Wei, M.; Saidaminov, M. I.; Gao, Y.; Xu, J.; Xiao, M.; Li, A.; Zhu, J.; Sargent, E. H.; Tan, H. Monolithic All-Perovskite Tandem Solar Cells with 24.8% Efficiency Exploiting Comproportionation to Suppress Sn(Ii) Oxidation in Precursor Ink. *Nature Energy* **2019**, *4* (10), 864–873. https://doi.org/10.1038/s41560-019-0466-3.
(15) Futscher, M. H.; Ehrler, B. Efficiency Limit of Perovskite/Si Tandem Solar Cells. *ACS Energy Lett.* **2016**, *1* (4), 863–868. https://doi.org/10.1021/acsenergylett.6b00405.
(16) Li, Z.; Zhao, Y.; Wang, X.; Sun, Y.; Zhao, Z.; Li, Y.; Zhou, H.; Chen, Q. Cost Analysis of Perovskite Tandem Photovoltaics. *Joule* **2018**, *2* (8), 1559–1572. https://doi.org/10.1016/j.joule.2018.05.001.

(17) Chen, H.; Maxwell, A.; Li, C.; Teale, S.; Chen, B.; Zhu, T.; Ugur, E.; Harrison, G.; Grater, L.; Wang, J.; Wang, Z.; Zeng, L.; Park, S. M.; Chen, L.; Serles, P.; Awni, R. A.; Subedi, B.; Zheng, X.; Xiao, C.; Podraza, N. J.; Filleter, T.; Liu, C.; Yang, Y.; Luther, J. M.; De Wolf, S.; Kanatzidis, M. G.; Yan, Y.; Sargent, E. H. Regulating Surface Potential Maximizes Voltage in All-Perovskite Tandems. *Nature* **2023**, *613* (7945), 676–681. https://doi.org/10.1038/s41586-022-05541-z.

(18) Thiesbrummel, J.; Peña-Camargo, F.; Brinkmann, K. O.; Gutierrez-Partida, E.; Yang, F.; Warby, J.; Albrecht, S.; Neher, D.; Riedl, T.; Snaith, H. J.; Stolterfoht, M.; Lang, F. Understanding and Minimizing VOC Losses in All-Perovskite Tandem Photovoltaics. *Advanced Energy Materials* **2022**, *n/a* (n/a), 2202674. https://doi.org/10.1002/aenm.202202674.

(19) Tong, J.; Jiang, Q.; Ferguson, A. J.; Palmstrom, A. F.; Wang, X.; Hao, J.; Dunfield, S. P.; Louks, A. E.; Harvey, S. P.; Li, C.; Lu, H.; France, R. M.; Johnson, S. A.; Zhang, F.; Yang, M.; Geisz, J. F.; McGehee, M. D.; Beard, M. C.; Yan, Y.; Kuciauskas, D.; Berry, J. J.; Zhu, K. Carrier Control in Sn–Pb Perovskites via 2D Cation Engineering for All-Perovskite Tandem Solar Cells with Improved Efficiency and Stability. *Nature Energy* **2022**, *7,* 642-651. https://doi.org/10.1038/s41560-022-01046-1.

(20) Lin, R.; Wang, Y.; Lu, Q.; Tang, B.; Li, J.; Gao, H.; Gao, Y.; Li, H.; Ding, C.; Wen, J.; Wu, P.; Liu, C.; Zhao, S.; Xiao, K.; Liu, Z.; Ma, C.; Deng, Y.; Li, L.; Fan, F.; Tan, H. All-Perovskite Tandem Solar Cells with 3D/3D Bilayer Perovskite Heterojunction. *Nature* **2023**, *620* (7976), 994–1000. https://doi.org/10.1038/s41586-023-06278-z.

(21) Zhang, M.; Lin, Z. Efficient Interconnecting Layers in Monolithic All-Perovskite Tandem Solar Cells. *Energy Environ. Sci.* **2022**, *15*, 3152-3170. https://doi.org/10.1039/D2EE00731B.

(22) Green, M. A.; Dunlop, E. D.; Yoshita, M.; Kopidakis, N.; Bothe, K.; Siefer, G.; Hao, X. Solar Cell Efficiency Tables (Version 62). *Progress in Photovoltaics: Research and Applications* **2023**, *31* (7), 651–663. https://doi.org/10.1002/pip.3726.

(23) Jošt, M.; Kegelmann, L.; Korte, L.; Albrecht, S. Monolithic Perovskite Tandem Solar Cells: A Review of the Present Status and Advanced Characterization Methods Toward 30% Efficiency. *Advanced Energy Materials* **2020**, *10* (26), 1904102. https://doi.org/10.1002/aenm.201904102.

(24) Guerrero, A.; Bisquert, J.; Garcia-Belmonte, G. Impedance Spectroscopy of Metal Halide Perovskite Solar Cells from the Perspective of Equivalent Circuits. *Chem. Rev.* **2021**, *121* (23), 14430–14484. https://doi.org/10.1021/acs.chemrev.1c00214.

(25) von Hauff, E.; Klotz, D. Impedance Spectroscopy for Perovskite Solar Cells: Characterisation, Analysis, and Diagnosis. *J. Mater. Chem. C* **2022**, *10* (2), 742–761. https://doi.org/10.1039/D1TC04727B.

(26) Pockett, A.; Eperon, G. E.; Peltola, T.; Snaith, H. J.; Walker, A.; Peter, L. M.; Cameron, P. J. Characterization of Planar Lead Halide Perovskite Solar Cells by Impedance Spectroscopy, Open-Circuit Photovoltage Decay, and Intensity-Modulated Photovoltage/Photocurrent Spectroscopy. *J. Phys. Chem. C* **2015**, *119* (7), 3456–3465. https://doi.org/10.1021/jp510837q.

(27) Zarazua, I.; Han, G.; Boix, P. P.; Mhaisalkar, S.; Fabregat-Santiago, F.; Mora-Seró, I.; Bisquert, J.; Garcia-Belmonte, G. Surface Recombination and Collection Efficiency in Perovskite Solar Cells from Impedance Analysis. *The Journal of Physical Chemistry Letters* **2016**, *7* (24), 5105–5113. https://doi.org/10.1021/acs.jpclett.6b02193.

(28) Gonzales, C.; Guerrero, A.; Bisquert, J. Transition from Capacitive to Inductive Hysteresis: A Neuron-Style Model to Correlate I–V Curves to Impedances of Metal Halide Perovskites. *J. Phys. Chem. C* **2022**, *126* (32), 13560–13578. https://doi.org/10.1021/acs.jpcc.2c02729.

(29) Guerrero, A.; Garcia-Belmonte, G.; Mora-Sero, I.; Bisquert, J.; Kang, Y. S.; Jacobsson, T. J.; Correa-Baena, J.-P.; Hagfeldt, A. Properties of Contact and Bulk Impedances in Hybrid Lead Halide Perovskite Solar Cells Including Inductive Loop Elements. *J. Phys. Chem. C* **2016**, *120* (15), 8023–8032. https://doi.org/10.1021/acs.jpcc.6b01728.

(30) Pockett, A.; Eperon, G. E.; Sakai, N.; Snaith, H. J.; Peter, L. M.; Cameron, P. J. Microseconds, Milliseconds and Seconds: Deconvoluting the Dynamic Behaviour of Planar Perovskite Solar Cells. *Phys. Chem. Chem. Phys.* **2017**, *19* (8), 5959–5970. https://doi.org/10.1039/C6CP08424A.

(31) Roose, B. Ion Migration Drives Self-Passivation in Perovskite Solar Cells and Is Enhanced by Light Soaking. *RSC Adv.* **2021**, *11* (20), 12095–12101. https://doi.org/10.1039/D1RA01166A.
(32) X. Chen; Y. Shirai; M. Yanagida; K. Miyano. Impedance Spectroscopy with Variable Voltages and Illuminations to Reveal Recombination Routes of Free Carriers in Perovskite Solar Cells. In *2019 IEEE 46th Photovoltaic Specialists Conference (PVSC)*; 2019; pp 0645–0647. https://doi.org/10.1109/PVSC40753.2019.8980871.
(33) Al-Ashouri, A.; Magomedov, A.; Roß, M.; Jošt, M.; Talaikis, M.; Chistiakova, G.; Bertram, T.; Márquez, J. A.; Köhnen, E.; Kasparavičius, E.; Levcenco, S.; Gil-Escrig, L.; Hages, C. J.; Schlatmann, R.; Rech, B.; Malinauskas, T.; Unold, T.; Kaufmann, C. A.; Korte, L.; Niaura, G.; Getautis, V.; Albrecht, S. Conformal Monolayer Contacts with Lossless Interfaces for Perovskite Single Junction and Monolithic Tandem Solar Cells. *Energy Environ. Sci.* **2019**, *12* (11), 3356–3369. https://doi.org/10.1039/C9EE02268F.
(34) Chiang, Y.-H.; Frohna, K.; Salway, H.; Abfalterer, A.; Pan, L.; Roose, B.; Anaya, M.; Stranks, S. D. Vacuum-Deposited Wide-Bandgap Perovskite for All-Perovskite Tandem Solar Cells. *ACS Energy Lett.* **2023**, *8* (6), 2728–2737. https://doi.org/10.1021/acsenergylett.3c00564.
(35) Bennett, L. J.; Riquelme, A. J.; Anta, J. A.; Courtier, N. E.; Richardson, G. Avoiding Ionic Interference in Computing the Ideality Factor for Perovskite Solar Cells and an Analytical Theory of Their Impedance-Spectroscopy Response. *Phys. Rev. Appl.* **2023**, *19* (1), 014061. https://doi.org/10.1103/PhysRevApplied.19.014061.
(36) Riquelme, A.; Bennett, L. J.; Courtier, N. E.; Wolf, M. J.; Contreras-Bernal, L.; Walker, A. B.; Richardson, G.; Anta, J. A. Identification of Recombination Losses and Charge Collection Efficiency in a Perovskite Solar Cell by Comparing Impedance Response to a Drift-Diffusion Model. *Nanoscale* **2020**, *12* (33), 17385–17398. https://doi.org/10.1039/D0NR03058A.
(37) Jacobs, D. A.; Shen, H.; Pfeffer, F.; Peng, J.; White, T. P.; Beck, F. J.; Catchpole, K. R. The Two Faces of Capacitance: New Interpretations for Electrical Impedance Measurements of Perovskite Solar Cells and Their Relation to Hysteresis. *Journal of Applied Physics* **2018**, *124* (22), 225702. https://doi.org/10.1063/1.5063259.
(38) Bisquert, J. Interpretation of the Recombination Lifetime in Halide Perovskite Devices by Correlated Techniques. *J. Phys. Chem. Lett.* **2022**, *13* (31), 7320–7335. https://doi.org/10.1021/acs.jpclett.2c01776.
(39) Zhang, L.; Kang, Q.; Shi, H.; Hong, J.; Song, Y.; Chi, D.; Huang, S.; He, G. Surface Defect Passivation of Pb–Sn-Alloyed Perovskite Film by 1,3-Propanediammonium Iodide toward High-Performance Photovoltaic Devices. *Solar RRL* **2021**, *5* (8), 2100299. https://doi.org/10.1002/solr.202100299.
(40) Albrecht, M. G.; Green, M. The Kinetics of the Photolysis of Thin Films of Lead Iodide. *Journal of Physics and Chemistry of Solids* **1977**, *38* (3), 297–306. https://doi.org/10.1016/0022-3697(77)90106-8.
(41) Dey, K.; Roose, B.; Stranks, S. D. Optoelectronic Properties of Low-Bandgap Halide Perovskites for Solar Cell Applications. *Advanced Materials* **2021**, *33* (40), 2102300. https://doi.org/10.1002/adma.202102300.
(42) Albina, A.; Taberna, P. L.; Cambronne, J. P.; Simon, P.; Flahaut, E.; Lebey, T. Impact of the Surface Roughness on the Electrical Capacitance. *Microelectronics Journal* **2006**, *37* (8), 752–758. https://doi.org/10.1016/j.mejo.2005.10.008.
(43) Domanski, K.; Correa-Baena, J.-P.; Mine, N.; Nazeeruddin, M. K.; Abate, A.; Saliba, M.; Tress, W.; Hagfeldt, A.; Grätzel, M. Not All That Glitters Is Gold: Metal-Migration-Induced Degradation in Perovskite Solar Cells. *ACS Nano* **2016**, *10* (6), 6306–6314. https://doi.org/10.1021/acsnano.6b02613.
(44) Shlenskaya, N. N.; Belich, N. A.; Grätzel, M.; Goodilin, E. A.; Tarasov, A. B. Light-Induced Reactivity of Gold and Hybrid Perovskite as a New Possible Degradation Mechanism in Perovskite Solar Cells. *J. Mater. Chem. A* **2018**, *6* (4), 1780–1786. https://doi.org/10.1039/C7TA10217H.

(45) Dey, K.; Ghosh, D.; Pilot, M.; Pering, S. R.; Roose, B.; Deswal, P.; Senananyak, S. P.; Cameron, P. J.; Islam, M. S.; Stranks, S. D. Substitution of Lead with Tin Suppresses Ionic Transport in Halide Perovskite Optoelectronics. arXiv: Condensed Matter > Materials Science, 3 May 2023. https://doi.org/10.48550/arXiv.2305.02014. (accessed 2023-08-08).
(46) Hu, S.; Otsuka, K.; Murdey, R.; Nakamura, T.; Truong, M. A.; Yamada, T.; Handa, T.; Matsuda, K.; Nakano, K.; Sato, A.; Marumoto, K.; Tajima, K.; Kanemitsu, Y.; Wakamiya, A. Optimized Carrier Extraction at Interfaces for 23.6% Efficient Tin–Lead Perovskite Solar Cells. *Energy Environ. Sci.* **2022**, *15* (5), 2096–2107. https://doi.org/10.1039/D2EE00288D.
(47) Frohna, K.; Anaya, M.; Macpherson, S.; Sung, J.; Doherty, T. A. S.; Chiang, Y.-H.; Winchester, A. J.; Orr, K. W. P.; Parker, J. E.; Quinn, P. D.; Dani, K. M.; Rao, A.; Stranks, S. D. Nanoscale Chemical Heterogeneity Dominates the Optoelectronic Response of Alloyed Perovskite Solar Cells. *Nature Nanotechnology* **2022**, *17* (2), 190–196. https://doi.org/10.1038/s41565-021-01019-7.